

High-throughput screening of bladder cancer exosome biomarkers by barcodes integrated herringbone microfluidics

Xiaowei Wei^a, Lijun Cai^{b,c,*}, Ning Li^b, Yile Fang^b, Jinglin Wang^{b,**}, Yefei Zhu^{a,***}

^a Laboratory Medicine Center, The Second Affiliated Hospital of Nanjing Medical University, Nanjing, 210011, China

^b Department of General Surgery, Nanjing Drum Tower Hospital, School of Biological Science and Medical Engineering, Southeast University, Nanjing, 210096, China

^c Department of Materials Science and Engineering, College of Design and Engineering, National University of Singapore, 117574, Singapore

ARTICLE INFO

Keywords:

Bladder cancer
Biomarker
Microfluidic chip
Photonic crystal
Encoding microcarrier

ABSTRACT

Bladder cancer (BC) ranks among the most prevalent urological malignancies with high mortality, driving an urgent need for efficient, non-invasive diagnostic methods. In this work, we developed an integrated microfluidic platform that combines herringbone mixers with photonic crystal (PhC)-encoded, core-shell hydrogel microcarriers for efficient exosome enrichment and multiplexed biomarker detection. The core-shell hydrogel microcarriers offer stable structural color barcoding immune to assay conditions and a substantially expanded surface area for enhanced sensitivity. Concurrently, the herringbone structures generate controlled microturbulence, significantly improving fluid mixing and extending target-probe contact time. By employing this platform to profile a panel of six proteomic biomarkers derived from bladder cancer exosomes, we demonstrate efficient high-throughput analysis of urinary exosomal signatures. The platform thus shows excellent diagnostic performance, offering a promising approach for the early detection and monitoring of BC in clinical practice.

1. Introduction

Exosomes, nanovesicles actively released by cells into the extracellular milieu, carry molecular cargos that reflect their originating cell membrane (Lone et al., 2022; Tran et al., 2021). The abundance of tumor-derived exosomes escalates with tumor progression, while it diminishes upon clinical remission (Hoshino et al., 2020; Kalluri and LeBleu, 2020). Consequently, protein biomarkers encapsulated within tumor-derived exosomes hold great potential as non-invasive indicators for early tumor detection and prognostic assessment (Maas et al., 2023; Tenchov et al., 2022; Yu et al., 2022). However, due to their low abundance in biological fluids, effective exosome enrichment and sensitive detection of their protein cargo are essential for extracting clinical diagnostic information (Kasiński et al., 2025; Sun et al., 2025). Although conventional techniques enable exosome isolation or single-target detection, the lack of integrated platforms for simultaneous enrichment and multiplexed protein profiling remains a critical barrier to advancing exosome-based diagnostics (Lone et al., 2022; Yang et al.,

2022). This limitation is particularly critical for heterogeneous diseases like bladder cancer, where a single biomarker often lacks the requisite sensitivity and specificity (Prip et al., 2025). Therefore, to build robust diagnostic models by capturing complementary molecular signatures through multiplexed exosomal protein profiling (Choi et al., 2024), it is imperative to create a novel bioassay system capable of both efficient enrichment and high-throughput multiplexed analysis, specifically for bladder cancer diagnosis (Spitzberg et al., 2023; Zhang et al., 2024a, 2024b).

Here, we propose a novel integrated approach utilizing a microfluidic chip combined with hydrogel barcodes to achieve both efficient exosome enrichment and multiplexed biomarker detection. Microfluidic technology, enabling precise manipulation of fluids at the microscale, offers superior solution kinetic performance compared to traditional solid-phase microarray chips (Sun et al., 2024; Ren et al., 2024; Wang et al., 2021). Notably, the herringbone microfluidic structure generates controlled microturbulence, significantly enhancing mixing efficiency and reaction kinetics (Sun et al., 2023; Ma et al., 2023; Skubal et al.,

* Corresponding author. Department of Materials Science and Engineering, College of Design and Engineering, National University of Singapore, 117574, Singapore.

** Corresponding author. Department of General Surgery, Nanjing Drum Tower Hospital, School of Biological Science and Medical Engineering, Southeast University, Nanjing, 210096, China.

*** Corresponding author. Laboratory Medicine Center, The Second Affiliated Hospital of Nanjing Medical University, Nanjing, 210011, China.

E-mail addresses: lijunca@nus.edu.sg (L. Cai), jinglinwang@njglyy.com (J. Wang), zhuyf@njmu.edu.cn (Y. Zhu).

<https://doi.org/10.1016/j.bios.2026.118545>

Received 21 November 2025; Received in revised form 27 January 2026; Accepted 16 February 2026

Available online 19 February 2026

0956-5663/© 2026 Elsevier B.V. All rights are reserved, including those for text and data mining, AI training, and similar technologies.

2025). Complementing this fluidic innovation, photonic crystal (PhC) barcodes provide stable structural color encoding that remains unaffected by reaction conditions (Hu et al., 2024a, 2024b; Wang et al., 2023; Zhang et al., 2022; Dadi and Ocoy, 2024). When engineered with a core-shell hydrogel architecture, these barcodes become ideally suited for liquid biopsy applications, with their expanded surface area substantially improving detection sensitivity (Zheng et al., 2024; Zhang et al., 2024a, 2024b; Hu et al., 2024a, 2024b). Critically, the integration of herringbone mixers with these encoded microcarriers within a single microfluidic device creates a synergistic effect. This unified approach addresses the interdependent challenges of inefficient particle-target contact in dilute samples and the need for multiplexed, surface-sensitive detection from limited clinical material.

In this study, we developed a high-throughput exosome biomarker detection system by integrating encoded microcarriers with herringbone microfluidic technology (Fig. 1). Using photonic crystal microparticles as templates, we constructed core-shell encoding microcarriers that exhibit enhanced affinity for exosome enrichment compared to conventional solid phase surfaces. Different biological probes were conjugated to the surface of distinctly colored barcode hydrogels, enabling simultaneous exosome capture and multiplex biomarker detection. The herringbone structures strategically positioned on the upper surface of the microfluidic chip effectively augment fluid resistance, induce controlled microturbulence, and consequently amplify the biological reaction interface while extending interaction time. When integrated into this microfluidic system, the hydrogel barcodes leverage their unique encoding properties and stable structural color signatures (unaffected by reaction conditions) to differentiate multiple exosomal protein biomarkers simultaneously. By employing proteomic analysis to identify differential biomarkers of bladder cancer exosomes, combined

with logistic regression and receiver operating characteristic (ROC) curves analysis, we demonstrate that this platform exhibits excellent diagnostic performance. Consequently, this integrated approach demonstrates significant potential for clinical translation in bladder cancer diagnosis and monitoring.

2. Results and discussion

2.1. Fabrication and characterization of core-shell encoding microcarriers

In a typical experiment, the core-shell encoding microcarriers were fabricated using photonic crystal microparticles as templates, produced from silica (SiO_2) nanoparticle-containing microfluidic droplets. These SiO_2 nanoparticle droplets were prepared by using silicone oil as the continuous phase and a suspension of monodisperse SiO_2 nanoparticles as the dispersed phase. Upon solvent evaporation at controlled temperature, the SiO_2 nanoparticles self-assembled into periodic ordered structures, forming photonic crystal microspheres (Fig. 2a and b). This distinctive physical architecture conferred photonic band gap properties to the microcarriers, thereby endowing them with encoding capabilities.

The self-assembled photonic crystal microparticles featured a characteristic nanoporous structure formed by the interstices between adjacent SiO_2 nanoparticles. To enhance the reaction surface area while minimizing background signal interference, we incorporated hydrogels into the nanoscale pores of the photonic crystal microparticles. The hydrogel precursor, comprising polyethylene glycol diacrylate (PEGDA) and polyethylene glycol (PEG), thoroughly infiltrates the nanoscale interstices of the photonic crystal template via capillary action, ensuring complete filling of the porous network (Fig. 2c). Subsequent UV-initiated polymerization rapidly solidifies the infused precursor into a

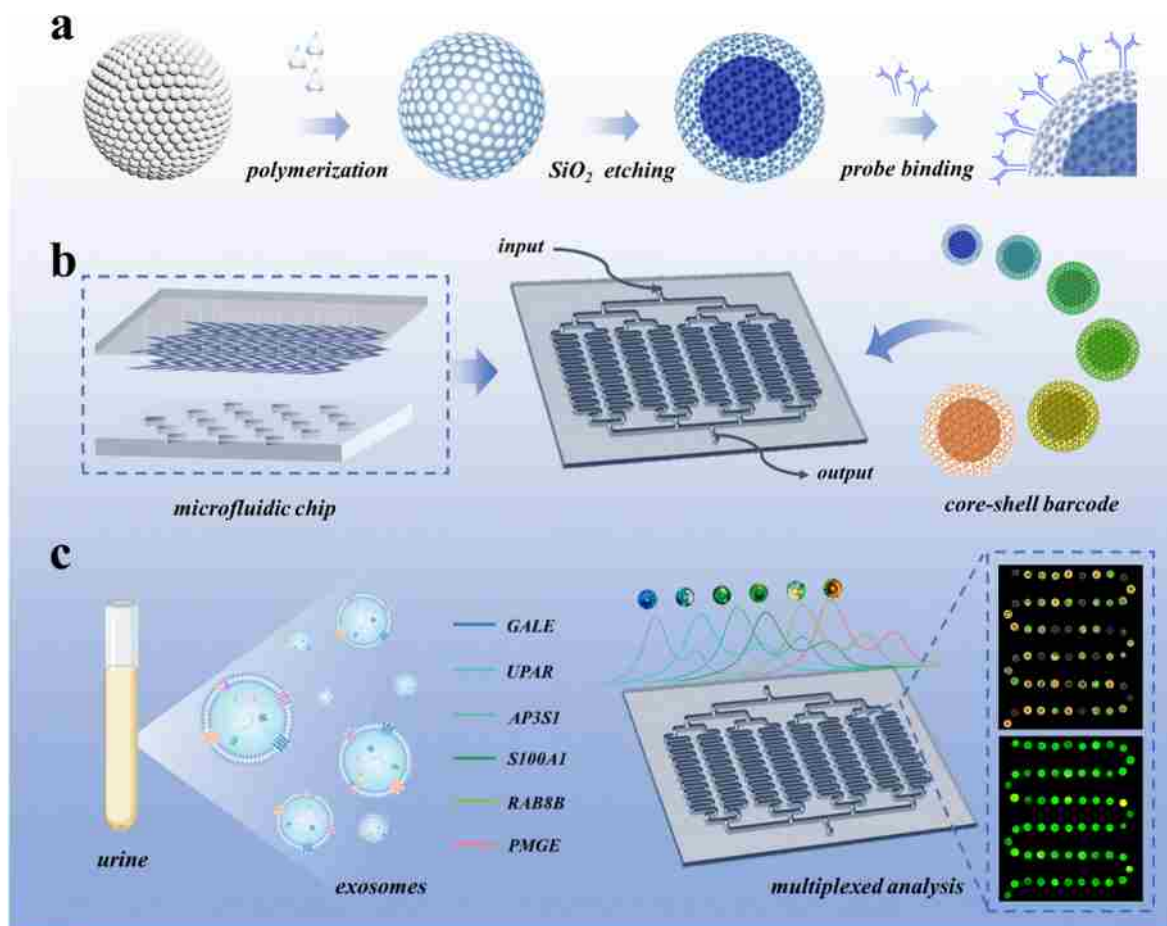


Fig. 1. Schematic illustration of the core-shell encoding microcarrier integrated microfluidic chip for multiplexed detection of BC-derived exosomal biomarkers.

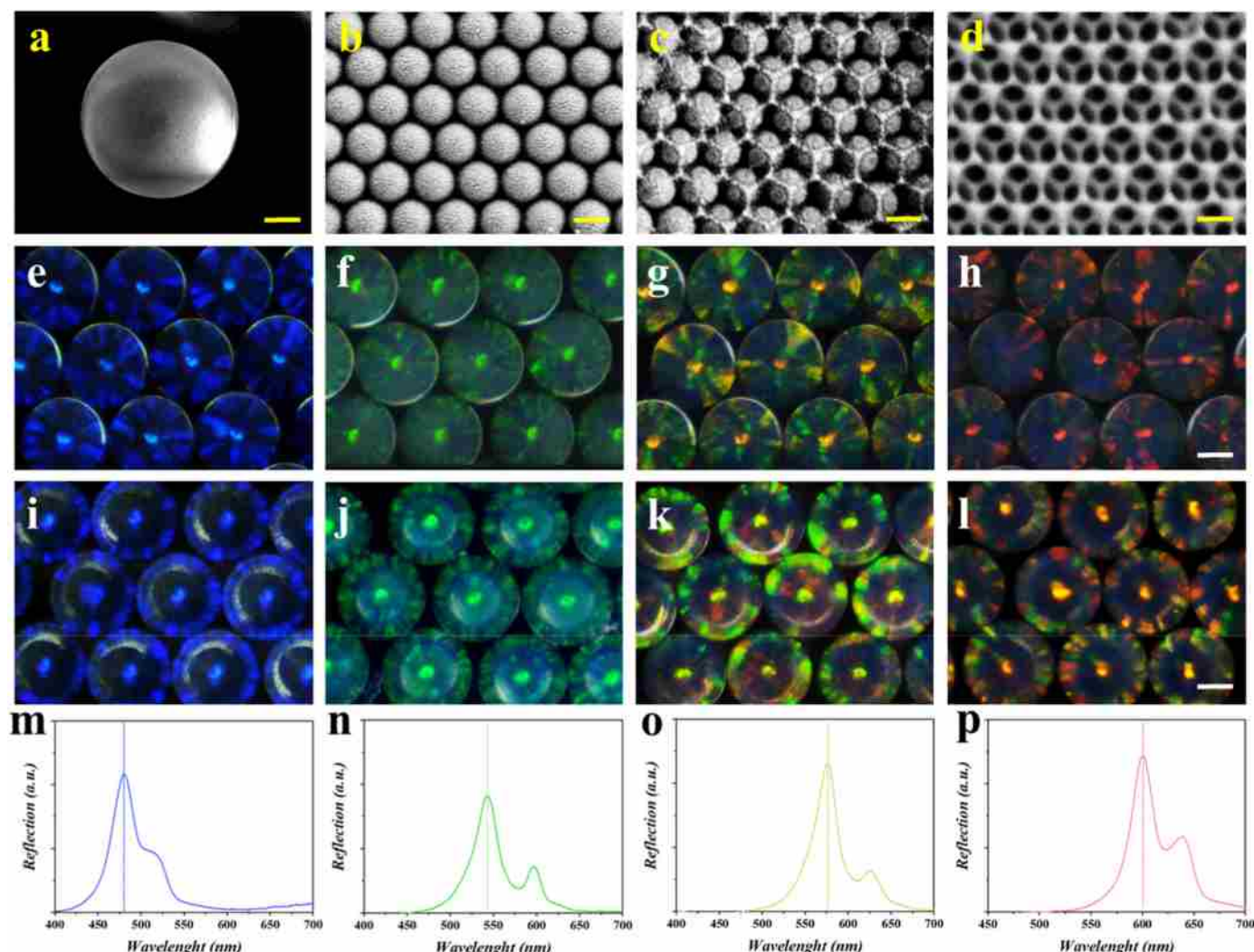


Fig. 2. Structural and spectral characterization of core-shell encoding microcarriers. (a-d) SEM characterization: (a) overall morphology of core-shell microcarrier (scale bar, 50 μm); (b) periodic ordered arrangement of nanoparticles in microcarrier core (scale bar, 200 nm); (c) nanoporous microcarriers with hydrogel infiltration (scale bar, 200 nm); (d) shell layer morphology after hydrofluoric acid etching (scale bar, 200 nm); (e-h) optical images of photonic crystal microcarriers with different colors (scale bar, 100 μm); (i-l) optical images of core-shell microcarriers (scale bar, 200 μm); (m-p) spectral characterization of core-shell hydrogel microcarriers demonstrating distinct reflectance peaks.

stable, cross-linked hydrogel matrix within the template, a transition confirmed by rheological measurements (Supplementary Fig. S1). Following polymerization, controlled surface etching with HF removes a defined outer layer, precisely shaping the final core-shell architecture that exhibits a well-defined inverse-opal shell structure (Fig. 2d).

This core-shell configuration augmented the surface area for enhanced biological reaction efficiency. Moreover, the preserved solid silica core limits deep penetration of molecules into the particle interior, confining interactions primarily to the more accessible and washable shell region, which helps reduce non-specific background interference. To objectively validate this advantage, we performed comparative experiments with varied etching depths. The results confirmed that core-shell design yields significantly lower background fluorescence than fully porous inverse-opal particles, as quantified in Supplementary Fig. S7 (Supplementary Information S1.2). The etching depth was systematically optimized to achieve an optimal balance between sufficient reactive surface area and controlled non-specific binding.

In contrast to the conventional use of antibody-conjugated solid microbeads for exosome capture, this engineered architecture combines a structurally encoded photonic crystal core with a functional hydrogel shell. The photonic crystal core provides stable, reaction-condition-

independent structural color for reliable multiplexed encoding, while the hydrogel shell significantly expands the accessible surface area for probe conjugation, enhancing capture capacity and detection sensitivity. Furthermore, the solid-core and porous-shell configuration effectively minimizes non-specific background by preventing the deep entrapment of molecules within interstitial gaps. This hybrid approach also surpasses pure hydrogel particles by maintaining the mechanical stability and precise optical properties of the photonic crystal template while leveraging the biocompatibility and high loading capacity of hydrogels, thereby simultaneously achieving enhanced enrichment efficiency and reliable multiplexed encoding.

The structural color properties of these microcarriers follow the optical diffraction law:

$$\lambda = 1.633d \cdot n_{\text{average}} \quad (1)$$

Derived from the periodic nanoarray characteristics and Bragg equation, where d represents the inter-particle distance between neighboring nanoparticle centers, and n_{average} denotes the average refractive index of the nanomaterials (Gregor et al., 2024). Under normal incidence, photonic crystal microcarriers constructed with varying nanoparticle dimensions exhibit distinct color signatures

(Fig. 2e–h). Consequently, the core-shell encoding microcarriers, utilizing photonic crystals as structural templates, maintain these periodic ordered physical structures and their associated structural color encoding characteristics (Fig. 2i–l), which serve as distinctive encoding elements for the microcarriers (Fig. 2m–p).

2.2. Optimization of probe conjugation conditions

In the preparation of core-shell encoding microcarriers, hydrogels containing acrylic acid (AA) were employed to functionalize their surface with abundant carboxyl groups. Subsequently, amino-modified probes were covalently conjugated to the microcarriers via carbodiimide coupling chemistry for specific exosome targeting. The preparation conditions were systematically optimized, including AA concentration, shell layer etching thickness, probe concentration, and target reaction time.

The AA concentration was found to directly influence the efficiency of probe immobilization. As demonstrated in Supplementary Fig. S2, an AA concentration of 20% (w/v) yielded optimal probe conjugation efficiency. Supplementary Figs. S3–S4 revealed that 4% (v/v) HF concentration provided an ideal balance between etching efficiency and etching rate manageability, resulting in a 50 μm (40% of total thickness) etching depth after 9 min of treatment. Furthermore, the relationship between fluorescence intensity and probe concentration was examined (Supplementary Fig. S5), establishing that probe molecule concentration of 0.1 μM resulted in detection signal saturation. The probe capture conjugation kinetics were also evaluated (Supplementary Fig. S6),

where the fluorescence signal reached plateau after 60 min of coupling reaction. Therefore, these conditions were selected as the optimal parameters for the analysis system.

2.3. Design and fluidic dynamics of microfluidic chip

Integration of core-shell microspheres into microfluidic platform Core-shell microspheres were integrated into microfluidic chips as flow microcarriers to quantify exosomal biomarkers for bladder cancer. The hydrodynamic mechanism of microfluidic technology enhances the efficiency of bioanalysis in liquid-phase coded chips (Zhou et al., 2024). The silicon chip model was fabricated using standard photolithography technology, with the structure replicated in polydimethylsiloxane (PDMS) due to its excellent chemical stability, thereby constructing a two-layer biomolecular reaction space (Fig. 3a and b).

Structural design for enhanced fluid dynamics The structural design incorporates a “V” convex protrusion at the top of the upper chip that increases fluid resistance, generating turbulence that drives comprehensive rotation of the microcarrier and extends the bioanalysis contact time (Fig. 3c). The “S” configuration serves as both the microfluidic flow channel and the transport pathway for encoding microcarriers, maximizing the biological reaction surface area. Additionally, the lower cylindrical “pit” structure facilitates precise positioning of encoding microcarriers, enabling rapid and accurate decoding during chip analysis (Fig. 3d). Our digital simulation of fluid flow lines within the microfluidic channel and its cross-section confirms that the integrated chip design creates sufficient resistance to generate effective

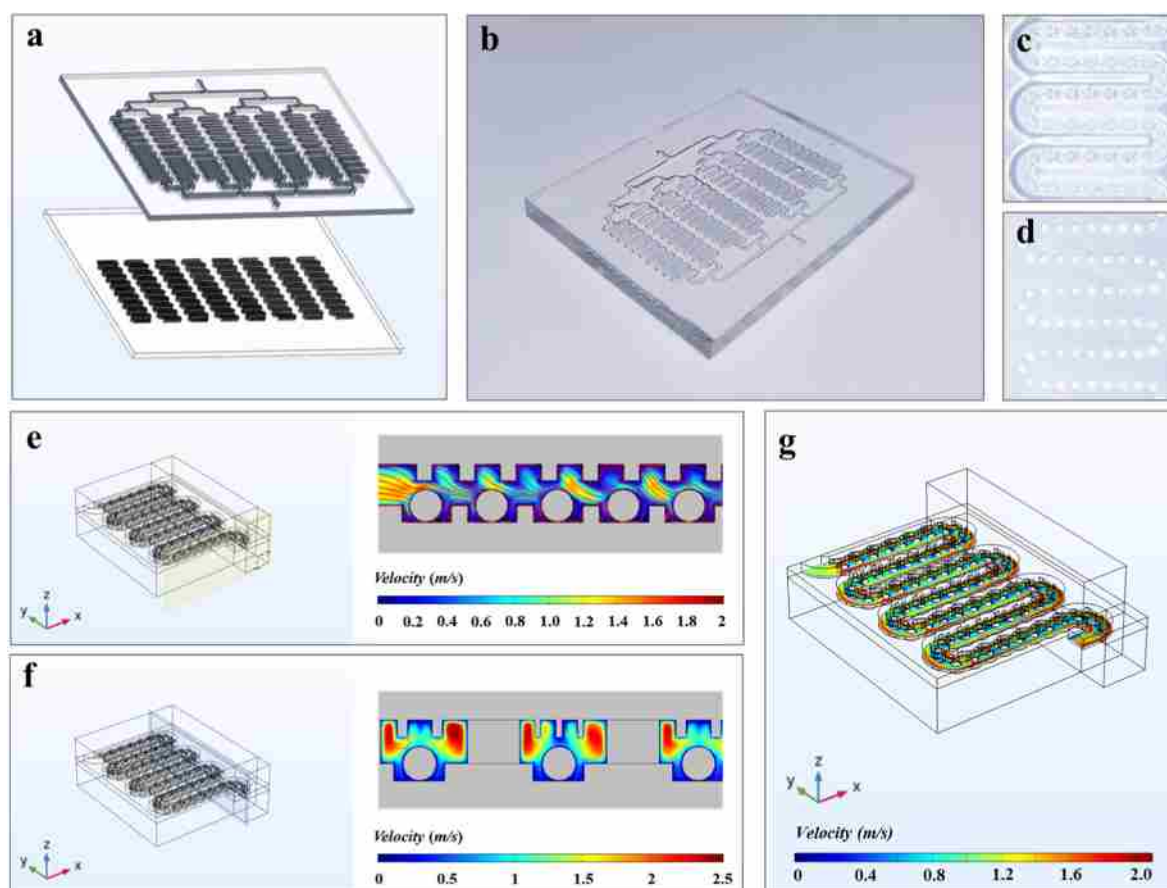


Fig. 3. Microfluidic chip design and fluid dynamics simulation. (a) Schematic illustration of the microfluidic chip architecture and (b) optical micrograph of the fabricated chip; (c) “V” shaped countercurrent design implemented to increase fluid resistance and enhance mixing efficiency; “S” shaped fluid channel for extended reaction time; (d) Cylindrical “pit” structure for precise positioning of microcarriers during analysis; (e) Microchannel longitudinal section with computational fluid dynamics simulation; (f) Microchannel cross-sectional flow line simulation demonstrating turbulent mixing patterns; (g) Streamline simulation of the turbulence intensity distribution on the herringbone microfluidic chip.

microfluidic turbulence (Fig. 3e and f; Supplementary Information S1.3). The flow rate of 1.8 mL/h was selected based on COMSOL streamline simulation and experimental validation to optimally balance mixing efficiency with sufficient interaction time for exosome-probe binding. This flow rate represents a compromise where the induced microturbulence is vigorous enough to enhance target-probe contact, yet the associated shear stress remains below a threshold known to preserve exosome integrity. At this optimized rate, streamline simulation analysis confirms that effective microturbulence is achieved across 70% of the chip area (Fig. 3g), which ensures uniform fluid mixing while minimizing shear-induced damage to exosome integrity (Supplementary Fig. S8).

Performance optimization and efficiency enhancement To optimize the analytical performance of our integrated platform, we

compared it against bare core-shell microcarriers. This comparative analyses revealed two key conferred by the microfluidic architecture: first, a significant enhancement in signal intensity under identical reaction conditions; and second, a substantial acceleration in the kinetics, reducing the time to reach signal saturation. To leverage these advantages, an operational flow rate of 1.8 mL/h was selected based on prior simulation and optimization. At this rate, the platform achieves a streamlined workflow wherein exosome capture reached saturation within ~45 min, and subsequent biomarker detection is completed in an additional ~35 min (Supplementary Fig. S9a and b). This dual-phase optimization underpins the system's capability for efficient, high-performance multiplexed analysis.

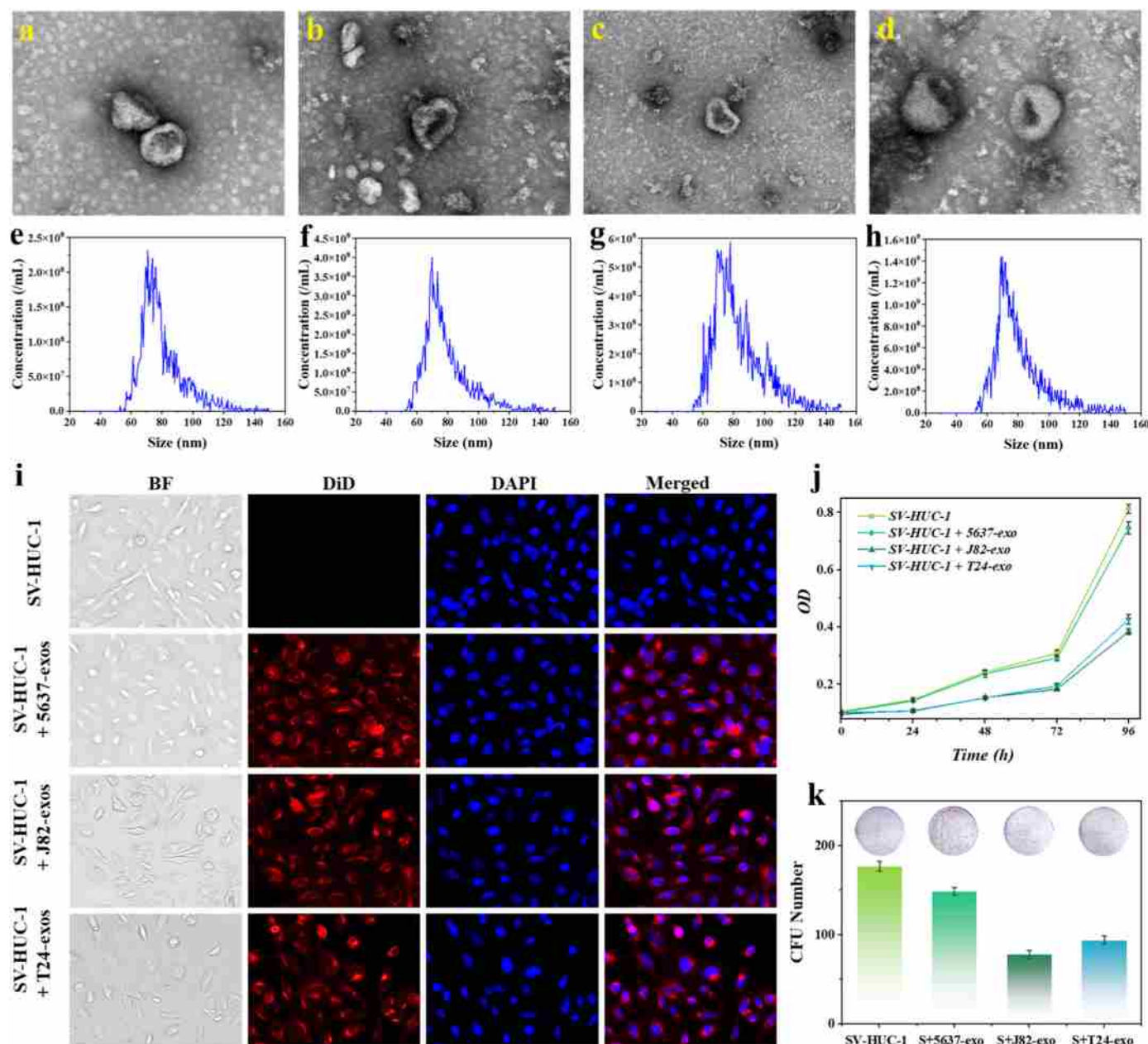


Fig. 4. Characterization and functional analysis of bladder cancer-derived exosomes. (a-d) TEM images of exosomes isolated from indicated cell lines (5637, T24, J82, and SV-HUC-1), displaying characteristic cup-shaped morphology (scale bar, 100 nm); (e-h) Size distribution profiles of exosomes measured by nano-flow cytometry (NanoFCM); (i) Fluorescence microscopy visualization of DiD-labeled exosome (red) internalization by SV-HUC-1 recipient cells; nuclei counterstained with DAPI (blue) (scale bar, 20 μ m); (j) Suppression of SV-HUC-1 cell proliferation demonstrated by CCK-8 assays following treatment with BC-derived exosomes ($P < 0.05$ vs. control; $n = 3$); (k) Differential inhibition of proliferative capacity by BC-derived exosomes assessed through colony formation assays.

2.4. Functional characterization of BC cell-derived exosomes

A foundational premise of our study is that exosomes used for biomarker discovery must be functionally active and representative of diverse tumor biology to capture the molecular heterogeneity of bladder cancer. Therefore, before proteomic profiling, we first established robust

cellular models and comprehensively characterized their secreted exosomes.

Selection and characterization of BC cell lines To efficiently identify tumor markers at cellular and molecular levels while avoiding the complexities of clinical sample heterogeneity, we selected BC cell lines with distinct biological characteristics: moderately differentiated

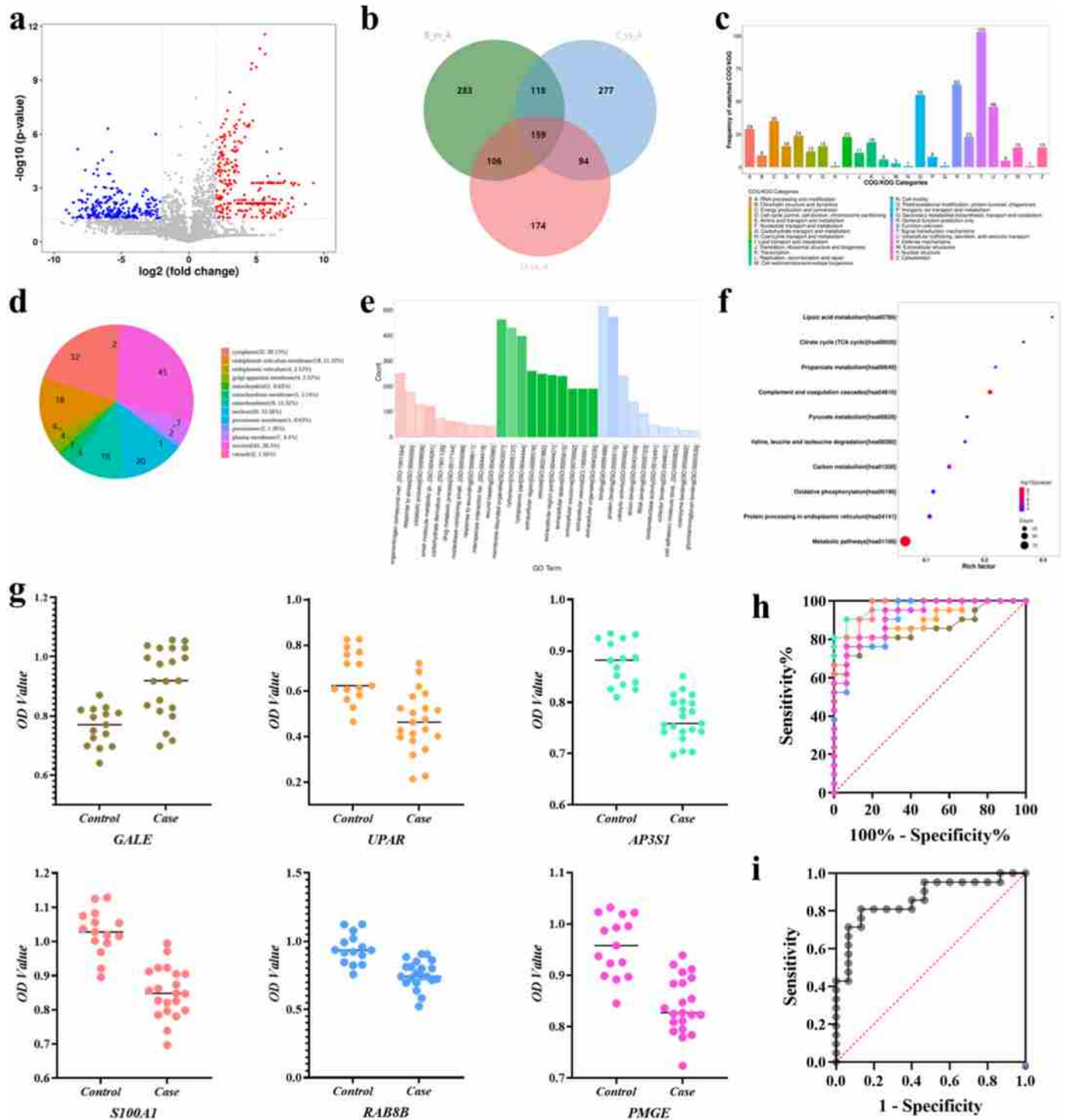


Fig. 5. Proteomic profiling and biomarker identification in bladder cancer-derived exosomes. (a) Volcano plot illustrating DEPs in BC-derived exosomes compared to non-cancer controls (Fold change ≥ 4 or ≤ 0.25 ; $P < 0.05$); (b) Venn diagram depicting the distribution and overlap of exosomal proteins among different BC cell lines (A: SV-HUC-1; B: 5637; C: J82; D: T24); (c) COG functional classification of DEPs; (d) Subcellular localization distribution of DEPs; (e) GO enrichment analysis showing significant association with exosomal compartments ($P < 0.001$); (f) KEGG pathway enrichment bubble plot (circle size: protein count; color: $\log_{10}(P\text{-value})$); (g) Logistic regression analysis of six candidate biomarkers in urine samples (BC: $n = 21$; non-cancer: $n = 15$); (h) ROC curves evaluating individual biomarker diagnostic performance; (i) ROC analysis of the combined 6-marker panel.

5637 cells and muscle-invasive T24 and J82 cells, with bladder epithelial SV-HUC-1 cells serving as controls. The CCK-8 assay and colony formation experiments demonstrated that BC cell lines exhibited significant proliferation advantages compared to SV-HUC-1 controls (Supplementary Fig. S10–S11). Migration and invasion capacities assessed through scratch and transwell assays revealed that 5637 cells displayed lower migration ability than the poorly differentiated T24 and J82 cells, which exhibited more aggressive behavior corresponding to their differentiation status (Supplementary Fig. S12–S15).

Isolation and characterization of exosomes from bladder cancer
Exosomes isolated from all cell lines via ultracentrifugation displayed the characteristic “cup-and-pan” morphology under transmission electron microscopy (TEM), with diameters within the expected 30–150 nm range (Fig. 4a–d). Nano-flow cytometry analysis demonstrated average particle sizes of 79.9 nm, 80.4 nm, 79.0 nm, and 83.2 nm for exosomes derived from 5637, T24, J82, and SV-HUC-1 cells, respectively (Fig. 4e–h). Western blot analysis confirmed the presence of canonical exosomal markers CD9, CD63, and CD81 (Supplementary Information S1.5; Supplementary Fig. S16).

Functional impact of bladder cancer exosomes on recipient cells
To assess biological activity, DiD-labeled BC-derived exosomes were incubated with recipient SV-HUC-1 cells. Fluorescence microscopy revealed efficient internalization of exosomes into the cytoplasm (Fig. 4i). Functional analysis demonstrated that treatment with BC-derived exosomes, particularly those from T2 and J82 cells, significantly suppressed the proliferation (Fig. 4j) and colony-formation ability (Fig. 4k) of SV-HUC-1 cells. Taken together, these results confirm that the isolated exosomes are biologically active vesicles capable of altering recipient cell behavior. This functional validation ensures that the subsequent proteomic profiling investigates molecular cargo derived from pathophysiologically relevant sources, thereby strengthening the biological rationale and clinical relevance of the discovered biomarkers.

2.5. Proteomic profiling and biomarker screening of BC-derived exosomes

Proteomic discovery and functional annotation of differential exosomal markers
Proteomic analysis of exosomes derived from for bladder cancer cell lines (5637, J82, T24) and non-malignant SV-HUC-1 cells identified 2938 proteins, with 2927 quantifiable. Using stringent criteria ($\text{Fold Change} \geq 4$ or ≤ 0.25 , $P < 0.05$ by Chi-square test), we identified 536 differentially expressed proteins (DEPs), including 279 up-regulated and 257 down-regulated proteins (Fig. 5a and b, Supplementary Fig. S17). Hierarchical cluster analysis visualized through heat maps demonstrated clear separation between BC cell groups and the NC group (Supplementary Information S1.6; Supplementary Fig. S18–S19).

COG (Cluster of Orthologous Groups) analysis revealed that DEPs were predominantly engaged in intracellular trafficking, secretion, vesicular transport, and signal transduction and posttranslational modification of proteins (Fig. 5c). Subcellular localization analysis indicated that DEPs were primarily distributed in the cytoplasm (29.13%), secreted compartment (24.17%), nucleus (18.47%), and plasma membrane (8.41%) (Fig. 5d). Gene Ontology (GO) annotation enrichment analysis confirmed exosomes as a major component containing DEPs in bladder cancer cells (Fig. 5e). KEGG pathway analysis demonstrated that metabolic pathways represented the largest category of DEPs (Fig. 5f), providing insights into the functional implications of these proteins in bladder cancer progression.

Selection and clinical validation of a multiplex biomarker panel
Based on comprehensive proteomic analysis and bioinformatic prioritization, we selected six candidate biomarkers: Galactose Epimerase (GALE), Urokinase-type Plasminogen Activator Receptor (UPAR), Adaptor Protein Complex 3 Sigma-1 Subunit (AP3S1), S100 Calcium Binding Protein A1 (S100A1), Ras-related Protein Rab-8B (RAB8B), and Prostate Membrane-specific Gene Enhancer (PMGE). A critical prerequisite for their detection in our integrated platform—which employs a

sandwich immunoassay targeting intact exosomes—is the presence of accessible epitopes on the exosomal surface. Database annotations (UniProt) and existing literature support the membrane association or surface localization of these candidates: UPAR is a glycosylphosphatidylinositol (GPI)-anchored receptor (Baart et al., 2021); RAB8B is a lipid-modified small GTPase targeted to vesicular membranes (Homma et al., 2021); AP3S1 is a subunit of the adaptor protein complex involved in membrane trafficking (Kong et al., 2024); S100A1 has been identified on the surface of exosomes and can bind to membrane receptors (Hua et al., 2020); GALE and PMGE have also been implicated in membrane-related processes or extracellular vesicle cargo (Zhao et al., 2024; Bakht et al., 2023). This confirms their suitability as direct targets for our surface-based detection assay.

To establish clinical relevance, we performed an independent validation using enzyme-linked immunosorbent assay (ELISA), a well-established quantitative method, on protein lysates derived from urinary exosomes of clinical samples. Clinical validation was performed using urine samples collected from patients at the Second Affiliated Hospital of Nanjing Medical University (Institutional Review Committee project [2024] KY-113-01) (Supplementary Table S1), with non-cancerous bladder conditions serving as controls. Exosomes were isolated from urine via ultracentrifugation, lysed, and analyzed by ELISA to quantify the expression levels of all six markers in both cohorts (Fig. 5g).

Diagnostic performance and rationale for the multi-marker strategy
The diagnostic performance of each individual marker was assessed using Logistic regression analysis, and similarly, the combined panel was evaluated through multivariate Logistic regression analysis (Supplementary Fig. S20–S21). Receiver operating characteristic (ROC) curves revealed AUC values of 0.5833, 0.6111, 0.7222, 0.7222, 0.75, and 0.5833 for GALE, UPAR, AP3S1, S100A1, RAB8B, and PMGE, respectively (Fig. 5h). The differential expression of this six-protein panel was confirmed in clinical urine samples using an independent, gold-standard ELISA, establishing its diagnostic relevance and providing a solid foundation for platform development. Therefore, the superior diagnostic performance of the combined panel ($\text{AUC} = 0.805$, Fig. 5i) over individual markers arises from the complementary biological information captured by the six proteins, which together reflect diverse pathological processes such as metabolic reprogramming, invasion, and immune modulation in bladder cancer. This multi-marker strategy effectively addresses tumor heterogeneity, a key challenge in single-analyte tests. While our exploratory model demonstrates promising utility, the integrated platform's inherent adaptability is crucial—it not only validates this initial panel but also provides a foundation for the future high-throughput refinement and optimization of biomarker signatures in larger, multi-center cohorts.

2.6. Multiplexed detection of exosome biomarkers using integrated microfluidic platform

Platform design and quantitative characterization
Leveraging the multiplexed encoding capability of photonic crystals and enhanced microfluidic dynamics, we constructed a high-throughput analysis platform by integrating functionalized core-shell microcarriers into the herringbone chip.

Leveraging the multiplexed encoding capability of photonic crystals and enhanced microfluidic dynamic, we constructed a high-throughput analysis platform by integrating functionalized core-shell microcarriers into the herringbone chips. Specific capture probes were conjugated to the microcarriers to target BC exosomal biomarkers, with Fluorescein Isothiocyanate (FITC) serving as the fluorescent readout for multiplexed, quantitative analysis (Kaur et al., 2024; Li et al., 2024) (Fig. 6a, Supplementary Fig. S22). The platform exhibited a concentration-dependent response, with signal intensity increasing significantly across exosome concentrations from 10^3 to 10^8 particles/mL (Fig. 6b). Using CD63 as the exosome marker, we established a correlation curve between exosome number and signal intensity,

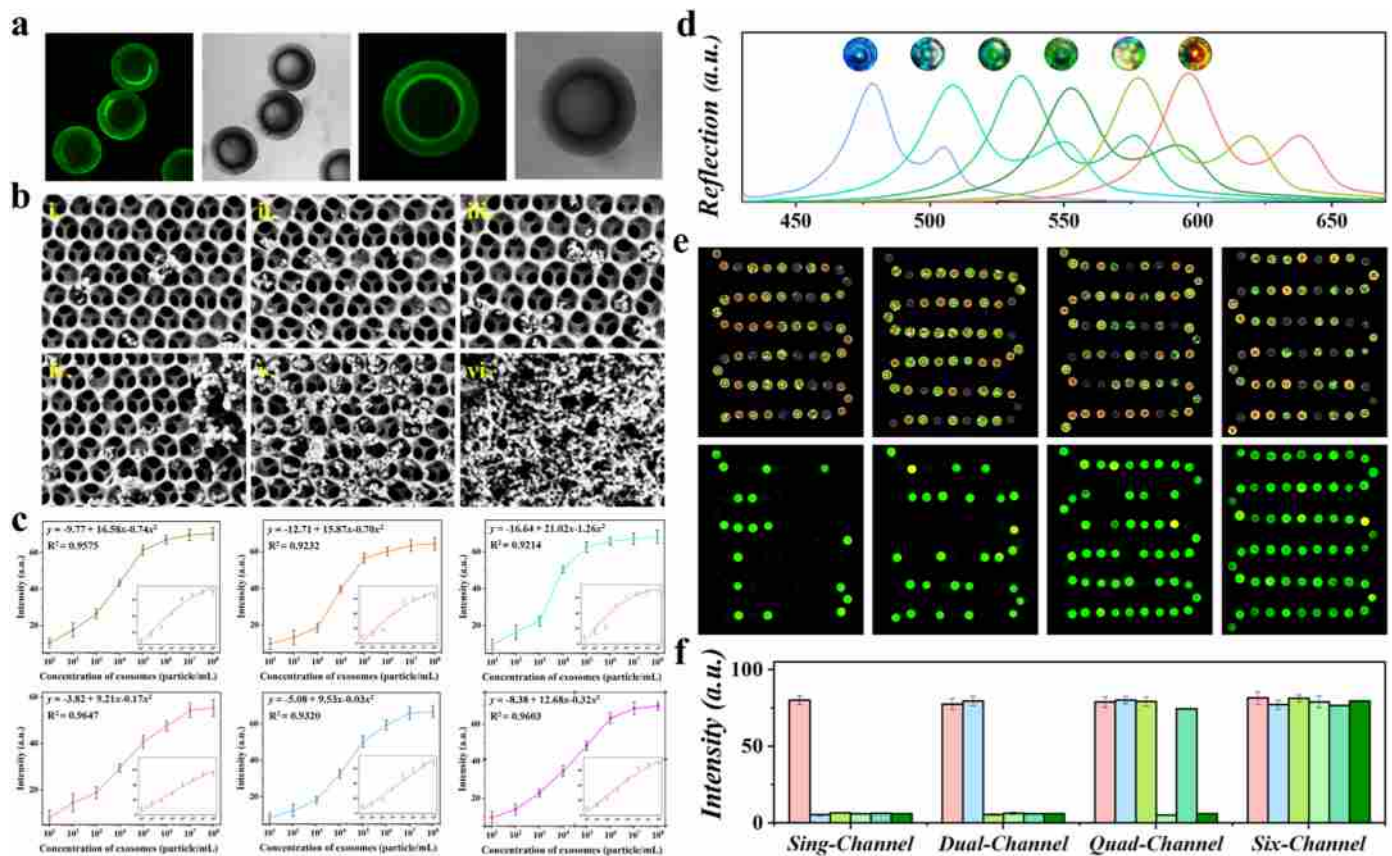


Fig. 6. Integrated microfluidic platform for multiplexed detection of bladder cancer exosomal biomarkers. (a) Confocal microscopy images demonstrating the optical and fluorescent imaging of core-shell microcarriers; (b) SEM images illustrating the exosome enrichment via core-shell microcarriers; (c) Quantitative detection curves of exosome-derived biomarkers; (d) Spectral characterization of core-shell microcarriers; (e-f) Multiplexed analysis of exosome-derived biomarkers using integrated chips: (e) multiplexed encoding and fluorescent decoding; (f) quantitative multiplexed analysis of fluorescence intensity.

yielding the equation $y = 4.43 + 2.55x - 0.47x^2$ (Supplementary Fig. S23), which better captures the saturation kinetics of exosome binding as the available capture sites on the microcarrier surface become occupied at higher concentrations.

The limit of detection (LOD) formula for optical analysis:

$$\text{LOD} = 3\sigma/S \quad (2)$$

Where S is the standard curve slope (equivalent to 95.21% confidence) and σ is the standard deviation of blank measurements, was as low as 10^3 particles/mL. Herein, a “measurable” signal is explicitly defined as exceeding the mean background signal by three times its standard deviation (3σ), which is the standard LOD criterion employed in Equation (2). This sensitivity is suitable for quantifying low-abundance targets in clinical samples.

Multiplexed profiling of the biomarker panel The integrated microfluidic chip system was employed for high-throughput composite analysis of BC-derived exosome markers GALE, UPAR, AP3S1, S100A1, RAB8B, and PMGE by calculating quantitative detection curves and R^2 values (Fig. 6c). The spectral encoding characteristics of the core-shell microcarriers enabled simultaneous identification of multiple biomarkers within a single detection assay (Fig. 6d). Through integrated encoding and fluorescent decoding strategies, each biomarker was assigned a unique spectral signature, facilitating accurate identification and multiplexed analysis (Fig. 6e). The measurable fluorescence intensity variations corresponding to different biomarker expression levels confirmed the system's analytical performance for quantitative multiplexed analysis (Fig. 6f).

Clinical validation using the integrated platform To directly evaluate clinical utility, we quantified the six biomarkers in the same

cohort of urine-derived exosomes using our platform. The resulting expression profiles are displayed a heatmap (Supplementary Fig. S24a). An ROC curve analysis based solely on the platform-generated data yielded an AUC of 0.798 (Supplementary Fig. S24b). This result closely aligns with the independent ELISA-based validation (AUC = 0.805), confirming the platform's capability to faithfully translate the multi-biomarker signature into a reliable diagnostic readout.

These results confirm that the integrated microfluidic chip with core-shell barcodes demonstrates robust diagnostic performance for bladder cancer. The platform features small sample volumes, high sensitivity, and streamlined multiplexed analysis, effectively simplifying the complex workflows associated with traditional exosome analysis, thus providing potential for clinical laboratory application.

3. Experimental section

3.1. Materials

Cell culture media and supplements, including exosome-depleted fetal bovine serum (FBS), RPMI-1640, high-glucose DMEM, MEM with NEAA, Ham's F-12K, trypsin-EDTA (0.25%), and Penicillin-Streptomycin were obtained from Gibco (USA). Polyethylene glycol diacrylate (PEGDA, average Mn 700), polyethylene glycol (PEG, average Mn 400), acrylic acid (AA), the photoinitiator 2-hydroxy-2-methylpropiophenone (HMPP), polydimethylsiloxane (PDMS, Sylgard 184), hydrofluoric acid (HF, 48%), methyl silicone oil (50 cSt), n-hexane and all buffer salts were purchased from Sigma-Aldrich (USA). Polyethylene glycol diacrylate (PEGDA, Mn 700), polyethylene glycol (PEG, Mn 400), acrylic acid (AA), the photoinitiator 2-hydroxy-2-methylpropiophenone

(HMPP), polydimethylsiloxane (PDMS), hydrofluoric acid (HF, 48%), and all buffer salts were purchased from Sigma-Aldrich (USA). Uranyl acetate dye solution was obtained from Yi Nationality Biotechnology Co., Ltd. (Shanghai, China). Primary capture antibodies against GALE, UPAR/PLAUR, AP3S1, S100A1, RAB8B and PSMA/FOLH1 were from Abcam (Cambridge, UK). Recombinant human proteins for calibration (GALE, AP3S1, S100A1, RAB8B, PSMA) were sourced from Sino Biological (Beijing, China); recombinant UPAR was from ACROBiosystems (Beijing, China). Fluorescein isothiocyanate (FITC)-conjugated detection antibodies were obtained from Absin (Shanghai, China). Methyl silicone oil 50 cSt and 500 cSt was obtained from Japan Tobacco (Japan). Ultrapure water used to prepare all buffer solutions was obtained from Millipore (Bedford, USA). All chemicals and reagents were of analytical grade or higher. Clinical urine samples were collected from patients at The Second Affiliated Hospital of Nanjing Medical University with informed consent, under a protocol approved by the hospital's Institutional Review Committee (Approval No. [2024] KY-113-01).

3.2. Preparation of core-shell encoding microcarriers

The fabrication of core-shell encoding microcarriers involved three sequential steps: template synthesis, hydrogel infiltration, and controlled etching. First, monodisperse silica nanoparticles synthesized via the Stöber method were assembled into photonic crystal microsphere templates using a droplet-based microfluidic device (Dadi and Ochoy, 2024). The detailed synthesis and assembly parameters are provided in **Supplementary Information S1.1**.

Subsequently, the calcined PhC templates were infiltrated under vacuum with a hydrogel precursor solution containing PEGDA (10% v/v), PEG (50% v/v), AA (20% v/v), and HMPP (1% v/v), followed by UV-induced polymerization to form a hydrogel-nanoparticle composite. Finally, controlled etching with hydrofluoric acid (HF) selectively removed the outer region, yielding a core-shell architecture with a solid silica core and a porous, carboxyl-rich hydrogel shell. The hydrogel formulation, polymerization conditions, and the systematic optimization of the HF etching process are described in **Supplementary Information S1.2**.

This design significantly increased the specific surface area for probe immobilization while confining biomolecular interactions to the accessible shell layer to minimize non-specific background.

3.3. Functionalization of microcarriers with capture probes

In this work, probe molecules were immobilized on the surface of microcarriers by chemical binding. The abundant carboxyl groups on the hydrogel shell (introduced by AA) were activated via EDC/NHS chemistry in MES buffer (pH 6.0). Amino-modified capture antibodies specific to the six target biomarkers (GALE, UPAR, AP3S1, S100A1, RAB8B, PMGE) were then covalently conjugated to the activated microcarriers (Zhou et al., 2022). The antibody concentration and conjugation time were systematically optimized to achieve maximal loading capacity and detection sensitivity. The specific protocols for surface activation and antibody conjugation are provided in **Supplementary Information S1.4**.

3.4. Design, fabrication and flow optimization of the herringbone microfluidic chip

The integrated microfluidic platform featured a two-layer PDMS architecture. The bottom layer contained an array of cylindrical micropits designed for precise positioning and retention of the encoding microcarriers. The top layer incorporated "V"-shaped herringbone mixer structures to induce controlled micro-scale turbulence, combined with an extended "S"-shaped main channel to prolong fluid-particle interaction time. The chip was fabricated via standard soft-lithography and irreversibly bonded using oxygen plasma treatment (Zhou et al., 2024).

The operational flow rate was selected based on computational fluid dynamics (CFD) simulations, which evaluated mixing efficiency and shear stress across a range of flow rates. A flow rate of 1.8 mL/h was chosen for subsequent experiments. The complete chip design, fabrication protocol, and simulation results are detailed in **Supplementary Information S1.3**.

3.5. Cell culture, exosome isolation and clinical sample processing

Human bladder cancer cell lines (5637, T24, and J82) with distinct differentiation statuses and the non-malignant uroepithelial cell line SV-HUC-1 were cultured in their respective media supplemented with 10% exosome-depleted FBS (Yang et al., 2023). Exosomes were isolated from conditioned cell culture media or clinical urine samples via differential ultracentrifugation. The isolated vesicles were characterized for size distribution using nano-flow cytometry (nFCM), morphology by transmission electron microscopy (TEM), and expression of canonical exosomal markers (CD9, CD63, CD81) by Western blot. For clinical validation, exosomes isolated from patient urine were lysed, and their protein content was quantified for parallel analysis by enzyme-linked immunosorbent assay (ELISA) and the integrated microfluidic platform. Detailed protocols for cell culture conditions, ultracentrifugation parameters, exosome characterization assays, and clinical sample handling are provided in **Supplementary Information S1.5**.

3.6. On-chip multiplexed detection of exosomal biomarkers

The detection was based on a sandwich immunoassay performed within the functionalized microfluidic chip. After system priming, exosome samples were introduced and allowed to be captured by the antibody-conjugated microcarriers. Following a wash step to remove unbound material, a mixture of fluorescein isothiocyanate (FITC)-conjugated detection antibodies was incubated with the captured exosomes. After a final wash, fluorescence signals from the individually encoded microcarriers were quantified in situ using a fiber-optic spectrometer. Quantification was performed by interpolating fluorescence intensities against calibration curves generated from recombinant protein standards for each biomarker. The complete step-by-step immunoassay protocol is provided in **Supplementary Information S1.4**.

3.7. Characterization methods

Structural, optical, and biophysical characterizations were performed using the following instruments. The morphology of the core-shell microcarriers and microfluidic chips was examined by scanning electron microscopy (SEM, Hitachi S-300N). Optical images were captured with a CCD camera (Olympus DP30BW). The structural color and reflection spectra of the encoding microcarriers were measured using a fiber-optic spectrometer (Ocean Optics HR2000). For exosomes characterization, morphology was assessed by transmission electron microscopy (TEM, Hitachi HT7700), and size distribution was analyzed by nano-flow cytometry (nFCM, FloCyto BS60000). Fluorescence imaging and intensity quantification for the multiplexed assay were performed using a fluorescence microscope (Olympus CKX41) coupled to the same fiber-optic spectrometer system. Fluorescence imaging and intensity quantification for the multiplexed assay were performed using a fluorescence microscope (Olympus CKX41) coupled to the same fiber-optic spectrometer system.

4. Conclusion

Bladder cancer diagnosis remains challenging due to tumor heterogeneity and the limited availability of highly sensitive non-invasive biomarkers. In this work, we have developed and validated a high-throughput screening system designed to address this need by integrating photonic crystal barcoded microcarriers with herringbone

microfluidic chip. This platform enables the efficient enrichment and multiplexed detection of exosomal proteins from urine samples. The core-shell microcarriers exhibited enhanced surface area for biomolecular capture and reduced background interference while maintaining stable structural color encoding properties under various reaction conditions. Proteomics analysis of exosomes from phenotypically distinct BC cell lines led to the identification of a six-biomarker panel. This multi-marker strategy, aimed at capturing complementary molecular signals to overcome the limitations of single-analyte tests, demonstrated a combined diagnostic AUC of 0.805 in our exploratory model, showing promising diagnostic utility. The integrated system achieved sensitive detection with significantly reduced reaction time due to the enhanced microturbulence and extended interaction periods between exosomes and capture probes within the microfluidic environment. This performance stems from a design philosophy that unites enhanced fluid dynamics, high-capacity encoded capture surfaces, and a streamlined workflow—effectively addressing the key limitations of stepwise or single-plex exosome analysis methods. The platform is versatile and provides a foundation for integrating future optimized biomarker panels. Therefore, with its non-invasive nature, high sensitivity, and multiplexing capability, this integrated system holds considerable potential to enhance the clinical diagnosis and monitoring of bladder cancer.

CRedit authorship contribution statement

Xiaowei Wei: Data curation, Formal analysis, Funding acquisition, Writing – original draft. **Lijun Cai:** Writing – review & editing. **Ning Li:** Data curation. **Yile Fang:** Data curation. **Jinglin Wang:** Methodology. **Yefei Zhu:** Conceptualization, Funding acquisition, Writing – review & editing.

Declaration of competing interest

The authors declare that they have no known competing financial interests or personal relationships that could have appeared to influence the work reported in this paper.

Acknowledgment

This work was supported by the Natural Science Foundation of Jiangsu (BK20220737), China Postdoctoral Science Foundation (2022M721404), “333 project” High-level Talent Cultivation Foundation of Jiangsu province (BRA2018086), and the Medical Research Project of Jiangsu Province Health Committee (K2019020).

Appendix A. Supplementary data

Supplementary data to this article can be found online at <https://doi.org/10.1016/j.bios.2026.118545>.

Data availability

Data will be made available on request.

References

- Baart, V.M., van der Horst, G., Deken, M.M., et al., 2021. A multimodal molecular imaging approach targeting urokinase plasminogen activator receptor for the diagnosis, resection and surveillance of urothelial cell carcinoma. *Eur. J. Cancer* 146, 11–20.
- Bakht, M.K., Yamada, Y., Ku, S.Y., et al., 2023. Landscape of prostate-specific membrane antigen heterogeneity and regulation in AR-positive and AR-negative metastatic prostate cancer. *Nat. Cancer* 4, 699–715.
- Choi, Y., Kim, S., Park, H., et al., 2024. Emerging multiplexed biosensing technologies for exosome analysis. *Adv. Sci.* 11, e2405187.
- Dadi, S., Ocsoy, I., 2024. Role of pretty nanoflowers as novel versatile analytical tools for sensing in biomedical and bioanalytical applications. *Smart Med* 3, e20230040.
- Gregor, P., Xin, Y., Paul, B., et al., 2024. Diamond-lattice photonic crystals assembled from DNA origami. *Science* 384, 781–785.
- Homma, Y., Hiragi, S., Fukuda, M., 2021. Rab family of small GTPases: an updated view on their regulation and functions. *FEBS J.* 288, 36–55.
- Hoshino, A., Kim, H.S., Bojmar, L., et al., 2020. Extracellular vesicle and particle biomarkers define multiple human cancers. *Cell* 182, 1044–1061.
- Hu, Y., Tian, Z., Ma, D., et al., 2024a. Smart colloidal photonic crystal sensors. *Adv. Colloid Interface Sci.* 324, 103089.
- Hu, Z., Qian, S., Zhao, Q., et al., 2024b. Engineering strategies for apoptotic bodies. *Smart Med* 3, e20240005.
- Hua, X., Zhang, H., Jia, J., et al., 2020. Roles of S100 family members in drug resistance in tumors: status and prospects. *Biomed. Pharmacother.* 127, 110156.
- Kalluri, R., LeBleu, V.S., 2020. The biology, function, and biomedical applications of exosomes. *Science* 367 eaau6977.
- Kasiński, A., Nowak, R., Wang, L., et al., 2025. Extracellular vesicles in cancer pathogenesis and diagnostics. *Trends Biotechnol.* 43, 112–125.
- Kaur, B., Kumar, S., Kaushik, B.K., 2024. Recent advancements in optical biosensors for cancer detection. *Biosens. Bioelectron.* 197, 113805.
- Kong, D., Wu, Y., Liu, Q., et al., 2024. Functional analysis and validation of oncoviral gene AP3S1 in ovarian cancer through filtering of mutation data from whole-exome sequencing. *Eur. J. Med. Res.* 29, 231.
- Li, Q., Zhan, S., Yang, X., et al., 2024. Choline phosphate-grafted nanozymes as universal extracellular vesicle probes for bladder cancer detection. *ACS Nano* 18, 16113–16125.
- Lone, S.N., Nisar, S., Masoodi, T., et al., 2022. Liquid biopsy: a step closer to transform diagnosis, prognosis and future of cancer treatments. *Mol. Cancer* 21, 79.
- Ma, Z., Fan, J., Wang, H., et al., 2023. Microfluidic approaches for microactuators: from fabrication, actuation, to functionalization. *Small* 19, e2300469.
- Maas, M., Todenhofer, T., Black, P.C., 2023. Urine biomarkers in bladder cancer-current status and future perspectives. *Nat. Rev. Urol.* 20, 597–614.
- Prip, F., Jensen, M.A., Lamy, P., et al., 2025. Molecular heterogeneity and evolution in bladder cancer subtypes. *Nat. Commun.* 16, 3456.
- Ren, H., Huang, D., Qiu, M., et al., 2024. Microfluidic 3D printing hydrogels based on fish liver decellularized extracellular matrix for liver regeneration. *Smart Med* 3, e20240056.
- Skubal, A., Zhang, Y., Nguyen, T., et al., 2025. Microfluidic platforms for high-throughput exosome analysis in oncology. *Lab Chip* 25, 1234–1245.
- Spitzberg, J.D., Ferguson, S., Yang, K.S., et al., 2023. Multiplexed analysis of EV reveals specific biomarker composition with diagnostic impact. *Nat. Commun.* 14, 1239.
- Sun, L., Chen, H., Xu, D., et al., 2024. Developing organs-on-chips for biomedical applications. *Smart Med* 3, e20240009.
- Sun, L., Wang, Y., Bian, F., et al., 2023. Bioinspired optical and electrical dual-responsive heart-on-a-chip for hormone testing. *Sci. Bull.* 68, 938–945.
- Sun, N., Wang, H., Li, Z., et al., 2025. Urinary exosomes as promising diagnostic biomarkers for bladder cancer. *Biosens. Bioelectron.* 208, 115203.
- Tenchov, R., Sasso, J.M., Wang, X., et al., 2022. Exosomes horizontal line nature's lipid nanoparticles, a rising star in drug delivery and diagnostics. *ACS Nano* 16, 17802–17846.
- Tran, L., Xiao, J.F., Agarwal, N., et al., 2021. Advances in bladder cancer biology and therapy. *Nat. Rev. Cancer* 21, 104–121.
- Wang, D., Liu, Z., Wang, H., et al., 2023. Structural color generation: from layered thin films to optical metasurfaces. *Nanophotonics* 12, 1019–1081.
- Wang, J., Ma, P., Kim, D.H., et al., 2021. Towards microfluidic-based exosome isolation and detection for tumor therapy. *Nano Today* 37, 101066.
- Yang, C., Ou, Y., Zhou, Q., et al., 2023. Methionine orchestrates the metabolism vulnerability in cisplatin resistant bladder cancer microenvironment. *Cell Death Dis.* 14, 525.
- Yang, C., Wu, S., Mou, Z., et al., 2022. Exosome-derived circTRPS1 promotes malignant phenotype and CD8⁺ T cell exhaustion in bladder cancer microenvironments. *Mol. Ther.* 30, 1054–1070.
- Yu, D., Li, Y., Wang, M., et al., 2022. Exosomes as a new frontier of cancer liquid biopsy. *Mol. Cancer* 21, 56.
- Zhang, P., de Haan, L.T., Debije, M.G., et al., 2022. Liquid crystal-based structural color actuators. *Light Sci. Appl.* 11, 248.
- Zhang, W., Hu, Y., Feng, P., et al., 2024a. Structural color colloidal photonic crystals for biomedical applications. *Adv. Sci.* 11, e2403173.
- Zhang, X., Chen, G., Wang, Y., et al., 2024b. Spatial tumor biopsy with fluorescence PCR microneedle array. *Innovation* 5, 100538.
- Zhao, Q., Li, B., Zhang, X., et al., 2024. M2 macrophage-derived lncRNA NORAD in EVs promotes NSCLC progression via miR-520g-3p/SMIM22/GALE axis. *npj Precis. Oncol.* 8, 185.
- Zheng, C., Wu, X., Liu, M., et al., 2024. Photothermal-enhanced in situ supramolecular hydrogel promotes bacteria-infected wound healing in diabetes. *Smart Med* 3, e20230047.
- Zhou, Q., Dong, K., Wei, M., et al., 2024. Rolling stone gathers moss: rolling microneedles generate Meta Microfluidic Microneedles (MMM). *Adv. Funct. Mater.* 34, 2316565.
- Zhou, Z., Yang, Z., Xia, L., et al., 2022. Construction of an enzyme-based all-fiber spr biosensor for detection of enantiomers. *Biosens. Bioelectron.* 198, 113836.